Research on Engineering Structures & Materials
www.jresm.org
Research Group

Research Article

Evaluation of bond strength between existing concrete and UHPC repair material using slant-shear tests with grooved and bar-anchored interfaces

Mohanad Natiq Alshandah [*,1,a], Zeyad Alshndah [1,b], Saba Muayad Mahmood [2,c]

[1]*Department of Civil Engineering, Tikrit University, Tikrit, Iraq*
[2]*Department of Dams and Water Resources, Tikrit University, Tikrit, Iraq*

Article Info

Article History:

Received 25 Sep 2026
Accepted 03 Nov 2026

Keywords:

Ultra-high-performance concrete;
Concrete repair;
Slant-shear;
Surface grooving;
Steel-bar anchorage;
Bond strength

Abstract

This study examined the peak-load bond-related response of existing C30 concrete repaired with ultra-high-performance concrete (UHPC) using inclined-interface compression tests. Eighteen composite specimens were tested at interface inclinations of 20°, 30°, and 40°, with three replicates per angle and interface configuration. The configurations comprised mechanically grooved interfaces without connectors (G-series) and nominally smooth interfaces incorporating 8 mm reinforcing bars (R-series). Peak axial forces were converted to nominal normal and shear stresses using angle-specific specimen areas. The G-series exhibited greater mean calculated shear stress than the R-series at each tested angle. At 30°, mean shear stresses were 12.65 and 10.91 MPa for G and R, respectively; at 40°, they were 14.27 and 11.56 MPa. Mohr–Coulomb regression was used to describe the peak-load stress states. Because specimen dimensions differed among angles and surface preparation was confounded with connector use, neither inclination nor treatment effects can be independently isolated. The results highlight the importance of interface preparation for the investigated UHPC repair configurations, while identifying the need for factorial testing and direct interface-slip measurements.

© 2026 MIM Research Group. All rights reserved.

1. Introduction

Repair of a concrete member is not simply a matter of removing the deteriorated material and replacing it with a higher-strength material. The extent of success of the repair strictly depends on the ability of the new material to act together with the aged cement concrete when loaded. In practice, this interaction is modulated through the interface, and any inadequacy in material property, surface or stress transfer may introduce cracking or separation. As a result, obtaining a strong bond is typically as critical as choosing a strong, durable repair material.

In recent years, ultra-high-performance concrete (UHPC) has received increasing attention as a potential rehabilitation material for deteriorated concrete members due to its high strength and low permeability as well as outstanding resistance to aggressive exposure environments. These characteristics and traits allow UHPC to be an attractive reparative material, especially when greater mechanical performance and longevity are essential. Nevertheless, just having a high-performance material in contact with the existing concrete does not guarantee a successful repair. Weakness in the interface may lead to failure along the bond plane prior to the full mobilization of the UHPC strength. Thus, the condition and preparation of the existing concrete surface are crucial for the overall performance of the repaired member.

*Corresponding author: dr.mohanad.alshandah@tu.edu.iq
[a]orcid.org/0009-0004-2254-9018; [b]orcid.org/0000-0002-3827-5574; [c]orcid.org/0009-0006-2769-7727
DOI: http://dx.doi.org/10.17515/resm2026-2403ma0925rs

Stress transfer at a concrete–UHPC interface involves multiple mechanisms. Previous studies indicate that adhesion, friction, and mechanical interlocking act cooperatively, and reinforcement that crosses the interface may offer additional resistance through dowel action. Surface geometry changes, such as in a grooved surface, encourage mechanical interlocking between two materials, while rebar acts as a more localized anchor. Further, the relative contribution of either mechanism may be a function of the stress state on the interface, such that a direct comparison under controlled conditions is informative. [1, 2].

Since axial compression naturally subjects an inclined bond plane to both normal and shear stresses across its area, the slant-shear test represents an appropriate system for such a comparison. Modification of the angle of this plane alters the ratio of these stress components and permits the assessment of the interface under various loading scenarios. Instead of using just the load at failure, Mohr–Coulomb criterion can be read at the corresponding normal and shear stresses and provide more insight on both the cohesive and frictional contributions to bond resistance.

Research gap and scope. Existing studies have investigated interface roughening, mechanical connectors, slant-shear geometry and frictional failure descriptions; however, comparisons across multiple inclination-dependent stress states are difficult to interpret when specimen geometry and interface treatment are not independently controlled. The present data are therefore evaluated as an exploratory comparison of two combined interface configurations, rather than a causal ranking of grooving and anchorage. The available studies collectively indicate that interface preparation, mechanical connectors, and imposed normal confinement influence bond resistance, but comparisons are complicated by differences in test geometry, loading and substrate treatment. In particular, independent quantification of groove geometry and connector action across multiple slant-shear angles remains limited. The present work addresses a narrower configuration-level gap by comparing grooved/unreinforced and nominally smooth/bar-anchored interfaces at three inclinations, while explicitly recognizing that the simultaneous change in interface treatment and specimen dimensions prevents independent causal attribution. Related experimental and review studies provide additional context on substrate condition, specimen size, test method, and interface response [3-13].

The present study examines two practical interface configurations under slant-shear loading at three inclinations. Its specific contribution is a configuration-level comparison of a grooved, unreinforced interface with a nominally smooth, bar-anchored interface, supported by replicate-level stress transformations and an explicit assessment of the limitations of Mohr–Coulomb regression. The study does not claim to identify the independent effects of surface roughness and bar anchorage, which would require a factorial experimental design.

2. Experimental Investigation

An experimental program was designed to measure bond behavior in the interface between an existing normal strength concrete substrate and a UHPC repair layer. Data were obtained from a slant-shear apparatus using a modified slant-shear arrangement to systematically vary the ratio of interfacial shear stress to normal compressive stress. Three interface angles, 20°, 30°, and 40° with respect to the normal loading axis, were studied. The reported test matrix contained two interface configurations: a mechanically grooved surface (G) and a nominally smooth surface incorporating an 8 mm-diameter steel anchorage bar (R). For each angle–interface combination, three nominally identical specimens were tested (i.e., three angles × two interfaces × three replicates = 18 composite specimens).

2.1 Material Properties

2.1.1 Cement

Ordinary Portland cement conforming to ASTM C150 Type I requirements was used in the C30 concrete substrate. The UHPC repair material incorporated the high-fineness Portland cement specified in the project data. Its comparatively high fineness was intended to promote hydration and contribute to the dense particle-packing system required for UHPC. For current Iraqi

specification terminology, IQS 5/2019 is used in place of the superseded 1984 designation. The measured chemical composition of the Portland cement is summarized in Table 1. The corresponding physical and mechanical cement properties are presented in Table 2.

Table 1. Chemical composition of the Portland cement used in the substrate concrete

Chemical Constituent / Parameter	Test Result
Calcium oxide, CaO	60.50%
Aluminium oxide, Al_2O_3	4.70%
Silicon dioxide, SiO_2	20.13%
Ferric oxide, Fe_2O_3	3.65%
Magnesium oxide, MgO	4.20%
Sulphur trioxide, SO_3	2.35%
Loss on ignition, LOI	2.75%
Insoluble residue	1.36%
Lime saturation factor, LSF	0.92

Table 2. Physical and mechanical properties of the Portland cement

Physical or mechanical property	Measured result	Iraqi Standard Specification IQS 5/2019
Blaine specific surface area	312 m^2/kg	≥230 m^2/kg
Initial setting time	2 h 18 min	≥45 min
Final setting time	4 h 12 min	≤10 h
3-day mortar compressive strength	295 kg/cm^2	≥150 kg/cm^2
7-day mortar compressive strength	347 kg/cm^2	≥230 kg/cm^2

The principal physical properties of the steel fibers are listed in Table 3. The adopted C30 substrate-concrete mixture proportions are given in Table 4. The UHPC mixture proportions used in the experimental program are reported in Table 5.

Table 3. Physical properties of steel fiber

Density (g/cm3)	Length(mm)	Diameter (mm)	Tensile Strength (MPa)	Modulus (GPa)
7.8	13	0.2	2950	200

Table 4. Concrete substrate mixes proportions (kg/m^3)

Strength grade	Cement	Water	River sand	Coarse aggregate
C30	325	140	725	1200

Table 5. UHPC mix proportions (kg/m^3)

Cement	Water	River sand	Silica fume	Steel fiber	SP
833.3	193.7	1041.6	208.3	152.9	31.03

2.1.2 Fine Aggregate

Natural washed river sand with a fineness modulus of 2.36 was used as the fine aggregate in the substrate concrete. The sand was clean and free from deleterious materials. In the UHPC matrix, conventional fine aggregate was replaced by high-purity quartz sand containing more than 99% SiO_2. The maximum quartz particle size was 0.60 mm, thereby limiting internal heterogeneity and improving matrix compactness.

2.1.3 Coarse Aggregate

Washed coarse aggregate with a nominal maximum particle size of 10 mm was incorporated in the C30 substrate concrete. Coarse aggregate was omitted from the UHPC repair mixture to obtain a

homogeneous, densely packed matrix and to facilitate penetration of the repair material into the prepared interface grooves.

2.1.4 Mixing Water

Clean potable water, free from substances that could adversely affect hydration or bond development, was used for mixing and curing. During production of the substrate concrete, the mixing water temperature was maintained within 20–25 °C. The UHPC mixture was proportioned with a nominal water-to-binder ratio (w/b) of 0.186, calculated from the reported mixing-water mass (193.7 kg/m^3) and total cementitious binder (833.3 kg/m^3 cement + 208.3 kg/m^3 silica fume). The corresponding water-to-cement ratio (w/c) is 0.232. These ratios are based on the tabulated batch quantities; any water contributed by liquid admixtures was not independently quantified, as stated in the experimental dataset.

2.1.5 Steel Reinforcement and Micro-Steel Fibers

Deformed steel bars with a nominal diameter of 8 mm were used as mechanical anchorage across the interface in the R-series specimens. The bars were positioned to cross the substrate–repair interface and were held securely during casting. The UHPC also contained high-strength micro-steel fibers with a tensile strength greater than 2000 MPa, a diameter of 0.15–0.25 mm, and a length of 6–13 mm. The fiber volume fraction was within 1.5–2.5%. The fibers were intended to control microcrack propagation and improve the tensile resistance and post-cracking integrity of the repair layer.

2.1.6 Silica Fume

Densified silica fume was incorporated in the UHPC at 25.0% of the cement mass. Its particle size was less than 0.10 μm. The silica fume served both as an ultrafine filler and as a highly reactive pozzolanic constituent, refining the pore structure and promoting additional calcium–silicate–hydrate formation.

2.1.7 High-Range Water-Reducing Admixture

A polycarboxylate-ether-based high-range water-reducing admixture was used in the substrate concrete. A fourth-generation superplasticizer developed for UHPC was used in the repair mixture. The admixture dosage was adjusted to provide a self-flowing, cohesive mixture at the very low water content without visible segregation or fiber balling. A consolidated comparison of the materials used in the substrate concrete and UHPC is provided in Table 6.

Table 6. Summary of materials used in the substrate concrete and UHPC repair material

Material	C30 substrate concrete	UHPC repair material
Cement	OPC, ASTM C150 Type I	High-fineness Portland cement; >400 m^2/kg
Fine fraction	Washed river sand; FM = 2.36	Quartz sand; >99% SiO_2; dmax = 0.60 mm
Coarse aggregate	Washed aggregate; dmax = 10 mm	Not used
Silica fume	Not reported	25.0% of cement mass; particle size <0.10 μm
Steel fibers	Not used	>2000 MPa; Ø0.15–0.25 mm; L = 6–13 mm; 1.5–2.5 vol.%
Chemical admixture	PCE high-range water reducer	Fourth-generation UHPC superplasticizer
Water ratio	Selected to achieve C30 target strength	w/b = 0.186 (from Table 5 masses)

2.1.8 Concrete Mixes

A single normal-strength substrate concrete was produced with a target 28-day compressive strength of 30 MPa (C30). The repair portion of each composite specimen was cast using the locally developed UHPC. The complete mixture proportions used in this experimental program are

reported in Tables 4 and 5. Interface inclination and interface preparation were treated as the experimental variables, while the substrate and repair materials were kept nominally constant.

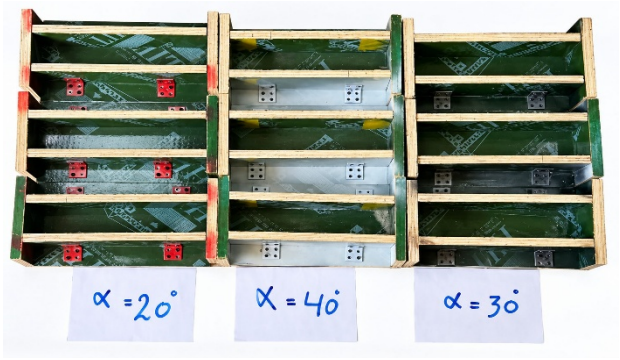
2.2 Sample Preparation

2.2.1 Molds and Specimen Geometry

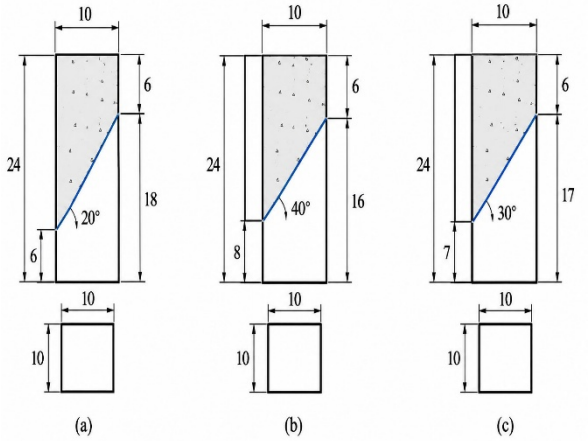
Moisture-resistant wooden moulds were fabricated with accurately positioned inclined partitions. Each partition defined the exposed substrate face at the prescribed angle to the vertical loading axis. All composite specimens were 200 mm high and had square cross-sections. Model A had a 62 × 62 mm cross-section with a 20° interface, Model B a 75 × 75 mm cross-section with a 30° interface, and Model C a 70 × 70 mm cross-section with a 40° interface. These dimensions were used in calculating the nominal axial stress and the corresponding normal and shear components. The custom mold arrangement and casting procedure are illustrated in Figure 1.



(a) Casting of the substrate halves in the inclined moulds



(b) Mould partitions arranged for α = 20°, 30°, and 40°



(c) Geometry of prism for slant shear test (a, b, and c) [mm]

Fig. 1. Preparation of the custom molds, casting of the inclined concrete substrates and Geometry of prism for slant shear test

Table 7. Specimen geometry for the investigated interface angles

Model	Interface angle, α	Square cross-section	Gross area, A	Overall height
A	20°	62 × 62 mm	3,844 mm^2	200 mm
B	30°	75 × 75 mm	5,625 mm^2	200 mm
C	40°	70 × 70 mm	4,900 mm^2	200 mm

The angle-specific specimen dimensions used in the stress calculations are summarized in Table 7. The angle-specific moulds led to different gross areas (3,844, 5,625 and 4,900 mm^2) and different height-to-width ratios. These dimensions were used in the original test program, but the available records do not document the design rationale. Normalizing by gross area permits nominal stress

comparison; it does not eliminate possible size, confinement and boundary effects. Thus, angle effects cannot be interpreted independently of specimen geometry.

2.2.2 Interface Preparation and Steel-Bar Details

For the G-series, regular grooves were formed across the inclined substrate face using a light electric chisel or rotary wire brush. The grooves were approximately 2–4 mm deep, with comparable widths, and were distributed as uniformly as practicable. For the R-series, the as-cast face was retained and cleaned with a soft brush, after which an 8 mm-diameter deformed steel bar was installed across the interface to provide mechanical anchorage. Representative substrate conditions before UHPC placement are shown in Figure 2.

The recorded groove depth was approximately 2–4 mm. Groove width and center-to-center spacing were not systematically measured or archived, and no sand-patch or profilometry roughness index was determined. These unmeasured geometric characteristics limit reproducibility and prevent a quantitative correlation between roughness and bond strength. Consequently, roughness should be treated as a qualitative configuration descriptor, and any claim of an independently quantified roughness effect is unwarranted.



(a) Cast substrate specimens with inclined interfaces

(b) Mechanically grooved substrate interfaces

Fig. 2. Representative substrate specimens before placement of the UHPC repair layer

The complete experimental matrix for the G- and R-series is summarized in Table 8.

Table 8. Interface configurations and experimental test matrix

Series	Interface condition	Angles	Replicates per angle	Total specimens
G	Mechanically grooved; grooves 2–4 mm deep and approximately equal in width	20°, 30°, 40°	3	9
R	Nominally smooth as-cast interface with Ø8 mm steel anchorage	20°, 30°, 40°	3	9
Total	—	—	—	18

2.2.3 Mixing, Surface Conditioning, and UHPC Placement

The dry constituents of the C30 concrete—cement, fine aggregate, and coarse aggregate—were first mixed for 2 min in a mechanical mixer operating at approximately 20–25 rpm. The mixing water and one-half of the pre-diluted superplasticizer were then introduced, and mixing continued for a further 2 min. The remaining superplasticizer was added during a final 1 min mixing period. The fresh concrete was placed in the prepared half-moulds and compacted on a calibrated vibration table at 50 Hz for 45 s.

The substrate halves were demolded after 24 h and immersed in water at 20 ± 2 °C for 28 days. The required interface treatment was then applied. Immediately before repair casting, the substrates

were immersed in clean water for an additional 24 h and subsequently exposed to laboratory air at 20 ± 2 °C and 60 ± 5% relative humidity for 30 min. The procedure achieved a saturated-surface-dry condition, preventing early wicking of mixing water away from the UHPC and the presence of free water at the bond plane.

The dry ingredients of UHPC, including cement, quartz sand, and silica fume, were premixed in a high-shear Hobart mixer under medium speed for 5 min. Superplasticizer and water were introduced incrementally, followed by 10 min of high-speed mixing until a homogeneous, viscous, self-flowing consistency was achieved. The micro-steel fibers were added to the mixture, which was then gradually dispersed in small batches at moderate speed for a further 4 min to minimize fiber agglomeration.

The mixing sequence was designed to produce the freshly mixed fiber-reinforced UHPC (fR-UHPC) (Figure 3). The visible fiber distribution was examined prior to placement, ensuring that concentrated fiber balls or dry pockets were not present in the mix. The appearance of the freshly mixed steel-fiber-reinforced UHPC is shown in Figure 3.



Fig. 3. Mixing and visual inspection of the fresh steel-fiber-reinforced UHPC

Each conditioned substrate half was returned to its corresponding mould, and the UHPC was placed in the remaining portion. The repaired specimens were vibrated for 15 s, which was sufficient to fill the grooves and local surface irregularities without causing fiber segregation. The completed composite specimens were then water-cured for an additional 28 days at 20 ± 2 °C before testing. Placement of the UHPC into the remaining inclined mould compartments is illustrated in Figure 4. Additional casting and mixing photographs are presented in Figure 7.



Fig. 4. Placement of the UHPC repair material in the remaining portions of the inclined moulds

2.3 Test Method

The composite specimens were tested under axial compression using a compression testing machine with a nominal capacity of 1000 kN. Each specimen was centered between rigid steel loading platens to minimize eccentricity. The laboratory equipment and calibration records should be retained as part of the experimental documentation. The specimens were loaded under force control at a constant axial loading rate of 2 kN/s (120 kN/min). Peak failure load was recorded for calculating nominal interfacial stresses. No LVDT or direct load–slip measurement was used. The

compression test setup is shown in Figure 8. The bar-anchored specimens are illustrated in Figure 6.

The maximum axial load at failure was recorded for each specimen. No external linear variable differential transformers (LVDTs) were installed, and no direct measurements of relative displacement or slip across the concrete–UHPC interface were obtained. Consequently, the experimental assessment is restricted to peak failure loads and the nominal interfacial normal and shear stresses calculated from these loads, specimen cross-sectional areas, and interface inclinations. Load–slip relationships, interfacial stiffness, post-peak response, and fracture energy cannot be evaluated from the available measurements. Representative post-test failure configurations are shown in Figure 9.

Material quality was monitored using 150 × 150 × 150 mm companion cubes produced from the relevant concrete batches. The 28-day compressive strength was determined to confirm the intended substrate class and the consistency of the repair material.

The 28-day compressive strength results for the three companion cubes of each material are presented in Table 9. The C30 substrate concrete achieved an average cube compressive strength of 33 MPa, exceeding its nominal target of 30 MPa. The UHPC repair material achieved an average cube compressive strength of 67 MPa. These measurements document the strengths of the tested companion cubes; they do not independently establish the bond performance of the composite specimens.

Table 9. Compressive strength of C30 and UHPC companion cubes at 28 days (MPa)

Specimen No.	C30 compressive strength (MPa)	UHPC compressive strength (MPa)
1	33	66
2	34	67
3	32	68
Mean	33	67

2.3.1 Interfacial Stress Evaluation

The peak axial load was converted into nominal axial stress using Eq. (4) and the measured gross cross-sectional area of the relevant model. Because the interface angle α was measured from the vertical loading axis, the normal compressive stress and shear stress acting on the inclined interface at failure were evaluated as follows: The representative inclined substrate profiles are shown in Figure 5.

$$\sigma_n = (P/A)\sin^2\alpha \quad (1)$$

$$\tau = (P/A)\sin\alpha\cos\alpha = (P/2A)\sin(2\alpha) \quad (2)$$

where P is the measured peak load (N), A is the corrected specimen cross-sectional area normal to the applied load (mm^2), α is the interface angle, σ_n is the compressive normal stress on the interface (MPa), and τ is the corresponding interfacial shear stress (MPa). Using a positive sign convention for compression, the strength envelope was represented by the linear Mohr–Coulomb relation:

$$\tau = c + \sigma_n \tan\varphi = c + \mu\sigma_n \quad (3)$$

$$\sigma_0 = P/A \quad (4)$$

$$\mu = \tan\varphi \quad (5)$$

$$\varphi = \tan^{-1}(\mu) \quad (6)$$

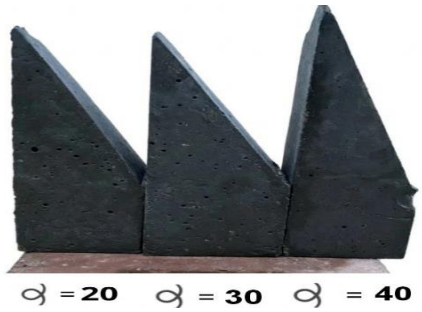
$$\tau/\sigma_n = \cot\alpha \quad (7)$$

In this expression, c is the apparent cohesion (MPa), φ is the interface friction angle, and μ is the friction coefficient [Eq. (5)]. Separate least-squares regressions of τ against σ_n were performed for

the G- and R-series. The intercept provided c, the slope provided μ, and φ was obtained from Eq. (6). The coefficient of determination (R^2) was used to assess the adequacy of the linear representation. Replicate results were retained to quantify test scatter, while the mean peak response at each inclination was used to compare the two interface-strengthening methods. For a fixed α, Eq. (7), so replicates at that angle occupy the same ray in stress space. Accordingly, the regression is exploratory: the three distinct angles provide the geometric variation, whereas the replicates characterize scatter and do not constitute independent stress-state directions.



(a) Representative smooth inclined faces



(b) Substrate profiles at α = 20°, 30°, and 40°

Fig. 5. Representative smooth inclined faces and substrate profiles at α = 20°, 30°, and 40°

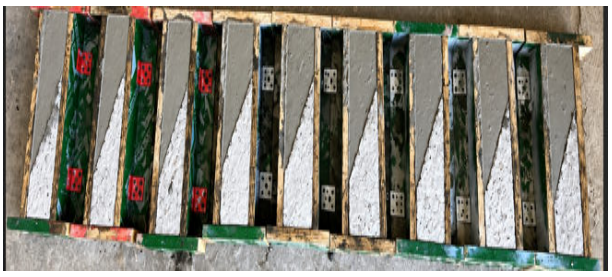


(a) Specimens prepared with crossing steel anchorage

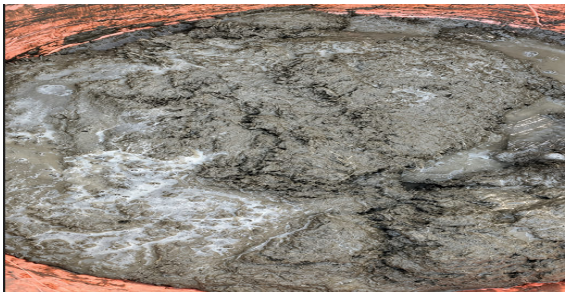


(b) Inclined substrate halves before repair casting

Fig. 6. Specimens prepared with crossing steel anchorage and inclined substrate halves before repair casting



(a) UHPC placement in the unfilled mould compartments



(b) Fresh UHPC during mixing immediately before casting

Fig. 7. UHPC placement and fresh UHPC mixing immediately before casting



Fig. 8. Composite specimens positioned in the testing machine at the investigated interface angles



Fig. 9. Representative specimen failure configurations after testing

3. Results and Discussion

3.1 Reported Mean Response

Table 10 summarizes nominal stresses recalculated from the confirmed peak failure forces (kN). These corrected values supersede the earlier values that inadvertently treated force magnitudes as axial stresses.

Table 10. Mean response of the investigated specimens

Angle	Interface	Mean σ_0 (MPa)	Mean τ_n (MPa)	Mean σ_n (MPa)
20	G	31.22	10.03	3.65
20	R	27.32	8.78	3.20
30	G	29.21	12.65	7.30
30	R	25.19	10.91	6.30
40	G	28.98	14.27	11.97
40	R	23.47	11.56	9.70

At each investigated inclination, the grooved (G) specimens developed higher mean nominal interfacial shear stresses than the bar-anchored (R) specimens (Table 10). Because specimen dimensions and interface configurations differ, these observations describe the tested configurations rather than isolated treatment effects.

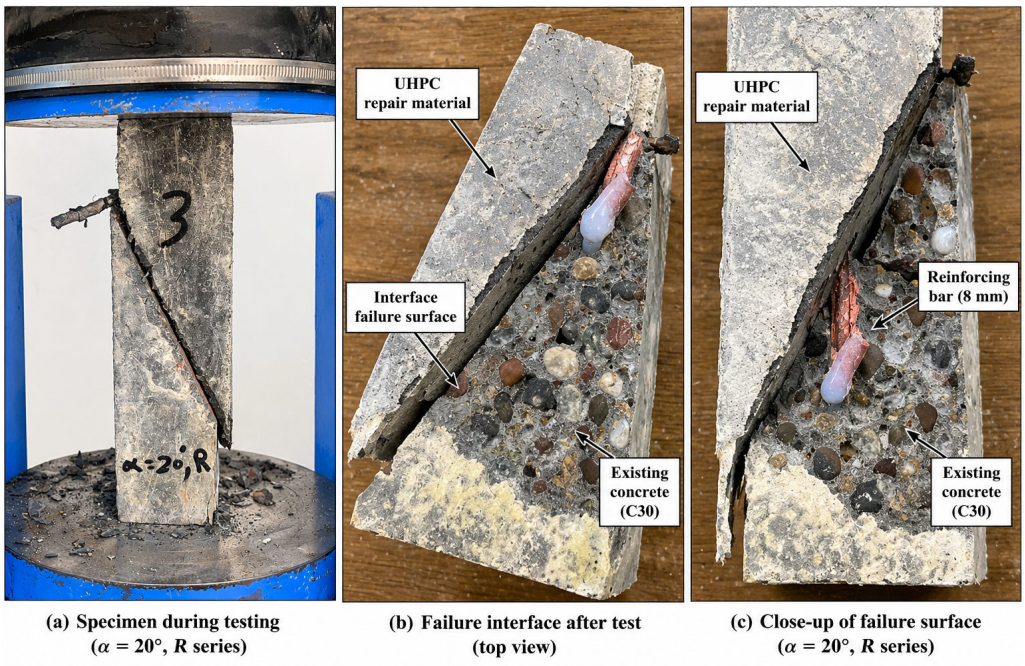
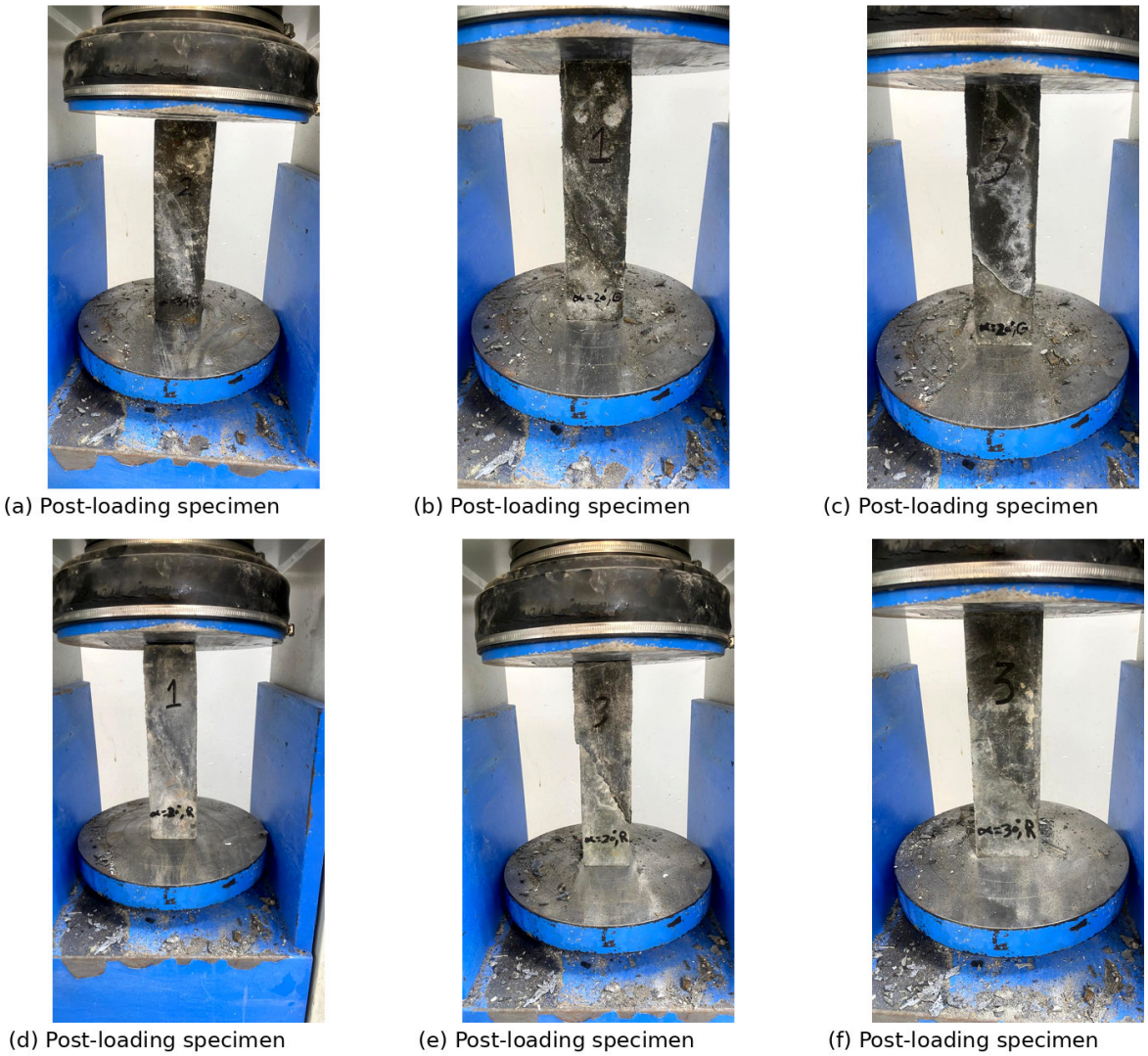


Figure 10. Representative photographic composite of a bar-anchored slant-shear specimen (20°) during and after testing

The figure is a visually enhanced illustration based on laboratory photographs; original images should be retained as primary experimental evidence.

The available photographs of the 20° bar-anchored specimen show a diagonal separation zone following the inclined interface, together with localized cracking and concrete fragmentation near the exposed reinforcing bar. These observations are consistent with predominantly interfacial separation accompanied by localized substrate damage in the photographed specimen. Because equivalent post-failure photographs and specimen-level observations are not yet available for every group, this observation is not generalized to all tested specimens. The representative photographic composite is shown in Figure 10, and additional post-loading images are presented in Figure 11. Representative post-loading specimen photographs (enhanced for visibility).



(a) Post-loading specimen (b) Post-loading specimen (c) Post-loading specimen

(d) Post-loading specimen (e) Post-loading specimen (f) Post-loading specimen

Fig. 11. Selected specimens photographed in the compression machine after loading

Contrast and sharpness were adjusted uniformly to improve visibility of surface cracking. Panel labels identify photographs only; exact specimen IDs and fracture-mode classifications require laboratory log verification.

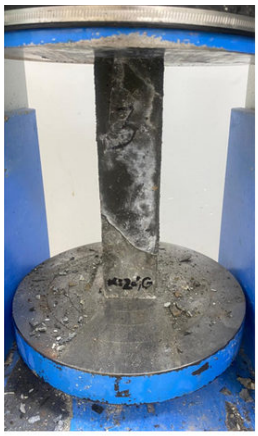
The following photographic plate compiles representative evidence supplied by the authors. Panels (b)–(d) document visible cracking after axial compression. These images alone do not establish the complete failure mechanism or identify every individual replicate. The grooved surface photograph shows substrate preparation, not a post-failure surface. The equipment labels are documentary evidence; full calibration certificates and the precise testing dates should be retained in laboratory records. The compiled photographic plate is presented in Figure 12.



(a) Grooved C30 substrate: prepared surface (pre-casting) (b) COSQC calibration label (photographic evidence)



(c) 20° specimen: visible post-loading cracking



(d) 30° specimen: visible post-loading cracking



(e) 40° specimen: visible post-loading cracking



(f) UTEST machine identification

Fig. 12. Representative grooved substrate, post-loading specimen appearances at nominal interface inclinations of 20°, 30° and 40°, UTEST machine branding, and COSQC calibration label

Image assignments should be cross-checked against laboratory specimen identifiers before publication.

3.2 Replicate-Level Mohr-Coulomb Data

Table 12 presents all 18 recalculated replicate-level stress pairs, based on the original peak force values and the corresponding specimen cross-sectional areas. The experimentally recorded peak failure loads for all 18 specimens are provided in Table 11 (kN), immediately before the corresponding calculated stresses in Table 12. The specimen-level stress pairs in Table 12 were calculated from the measured peak loads in Table 11 using Eqs. (1) and (2). Each angle defines a fixed shear-to-normal-stress ratio; replicate observations quantify within-group variation.

Table 11. Original peak failure loads (kN) for the grooved (G) and reinforcing-bar-anchored (R) specimens

Angle (°)	Interface	Peak load 1 (kN)	Peak load 2 (kN)	Peak load 3 (kN)
20	G	125	115	120
20	R	110	105	100
30	G	163	170	160
30	R	150	140	135
40	G	146	130	150
40	R	120	110	115

Table 12. Replicate-level normal and shear stress data

Angle	Interface	σ_n (MPa)	τ_n (MPa)
20	G	3.80	10.45
20	G	3.50	9.62
20	G	3.65	10.03
20	R	3.35	9.20
20	R	3.20	8.78
20	R	3.04	8.36
30	G	7.24	12.55
30	G	7.56	13.09
30	G	7.11	12.32
30	R	6.67	11.55
30	R	6.22	10.78
30	R	6.00	10.39
40	G	12.31	14.67
40	G	10.96	13.06
40	G	12.65	15.07
40	R	10.12	12.06
40	R	9.28	11.05
40	R	9.70	11.56

3.3 Repeatability of the Axial Failure Stress

Repeatability statistics for axial failure stress are summarized in Table 13. The angle-dependent mean response and error bars are shown in Figure 13.

Table 13. Statistical repeatability of the reported replicate axial failure stresses (SD and CV)

Angle	Interface	Mean σ_0	SD	CV (%)
20	G	31.22	1.30	4.17
20	R	27.32	1.30	4.76
30	G	29.21	0.91	3.12
30	R	25.19	1.36	5.39
40	G	28.98	2.16	7.45
40	R	23.47	1.02	4.35

Figure 13 displays the angle-dependent mean axial failure stress with ±1 standard deviation for each configuration. The variation reported in Table 13 should be interpreted alongside the different prism dimensions.

3.4 Effect of Interface Configuration and Angle

The angle-dependent mean axial failure stresses and their standard deviations are presented in Figure 13. The separate G- and R-series Mohr–Coulomb regression lines are presented in Figure 14, and the combined experimental stress response with its pooled fit is shown in Figure 15.

Figure 14 compares the separately fitted Mohr–Coulomb envelopes for the G- and R-series. The difference between these fitted trends is descriptive because surface roughening and connector installation were not varied independently. Figure 15 presents the combined experimental stress pairs and the pooled regression. This pooled envelope summarizes the investigated configurations but is not a validated interface design criterion.

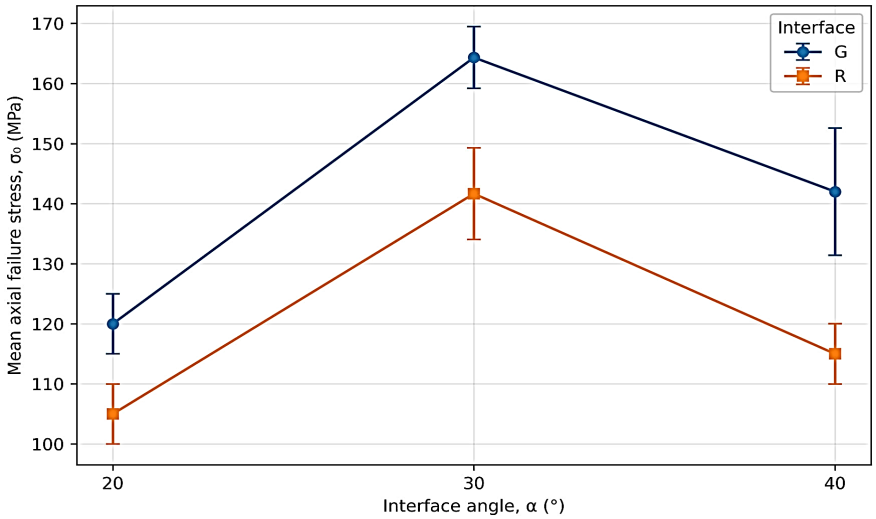


Fig. 13. Mean axial failure stress as a function of interface angle for the G- and R-series; error bars represent ±1 SD (n = 3)

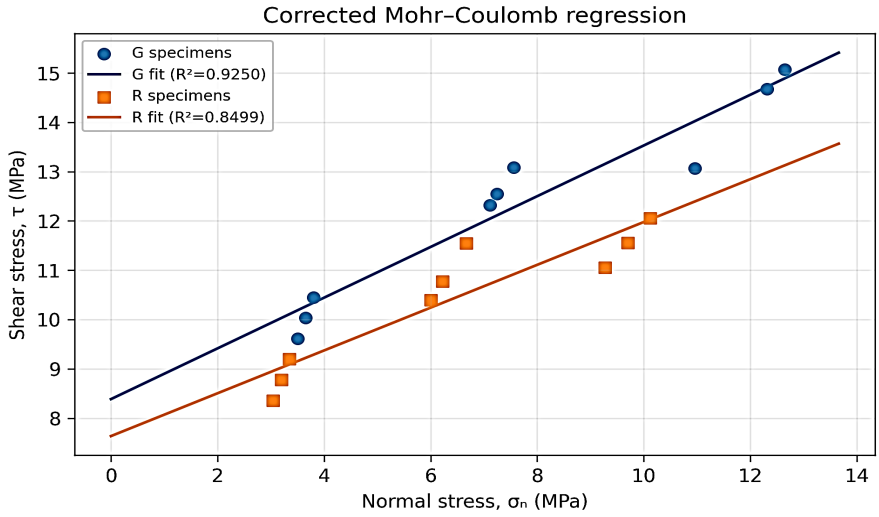


Fig. 14. Mohr–Coulomb representation of replicate-level experimental data and fitted regression lines for the G- and R-series

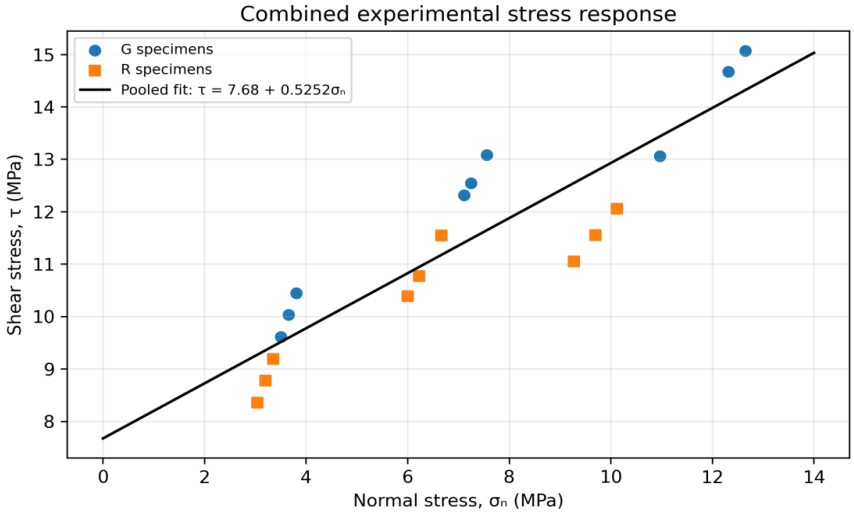


Fig. 15. Combined experimental response used for Mohr–Coulomb interpretation

3.5 Mohr-Coulomb Failure Envelope

The corrected pooled least-squares regression of the 18 specimen-level stress pairs is given by Eq. (8), with $R^2 = 0.8032$. This supersedes the earlier pooled fit based on incorrectly interpreted load units. The corrected group regressions are G: c = 8.39 MPa, μ = 0.5142, φ = 27.21°, $R^2 = 0.9250$; R: c = 7.64 MPa, μ = 0.4340, φ = 23.46°, $R^2 = 0.8499$. The fitted stress envelopes are illustrated in Figure 14.

$$\tau = 7.68 + 0.5252\sigma_n \ (MPa) \tag{8}$$

The combined experimental stress response and pooled regression line are shown in Figure 15; the group-specific regression lines are shown in Figure 14. The pooled and treatment-specific Mohr–Coulomb parameters are summarized in Table 14.

Table 14. Mohr-Coulomb parameters from the pooled regression and treatment-specific secondary regressions

Dataset	c (MPa)	μ = tanφ	φ (deg)	R^2
All G + R (pooled)	7.68	0.5252	27.71	0.8032
G only	8.39	0.5142	27.21	0.9250
R only	7.64	0.4340	23.46	0.8499

3.6 Effect of Interface Angle

Across the tested angles, the calculated nominal normal and shear stress components vary with inclination according to Eqs. (1) and (2). However, the accompanying change in prism cross-section prevents a causal assessment of inclination alone.

3.7 Effect of Interface Preparation

The G-series consistently exhibited higher mean peak-load-derived shear stress than the R-series (Table 10). This result pertains to grooved interfaces without connectors versus nominally smooth interfaces with 8 mm connectors; it cannot isolate roughness from dowel action.

3.8 Effect of Reinforcing-Bar Anchorage

The lower response of the R-series should not be interpreted as evidence that steel connectors are inherently detrimental. In the present experimental program, the R-series combined a steel connector with an otherwise smooth interface, whereas the G-series combined deliberate roughening with no connector. Two variables therefore changed simultaneously. The observed difference may reflect limited distributed interlock on the smooth surface, local stress concentrations around the connector, splitting or bearing damage, or interaction between connector slip and interface debonding. A more comprehensive factorial experimental program incorporating smooth interfaces with and without connectors and roughened interfaces with and without connectors would be necessary to distinguish the individual contribution of surface roughness from that of reinforcing-bar dowel action, as well as to identify any interaction between the two mechanisms. This distinction is particularly relevant when the present findings are considered alongside recent investigations. [14], for example, evaluated UHPC–NSC interfaces prepared using smooth, chipped, and steel-wire-mesh treatments, highlighting the importance of interface condition in governing composite bond behavior. More recently, Morthala and Shanmugam [15] investigated grooved, shear-link-reinforced, and water-pressure-jetted interfaces through slant-shear tests conducted at different interface inclinations, together with splitting tensile tests. Their findings indicate that connector-assisted interfaces can develop substantial bond resistance when the surrounding surface condition, connector detailing, and associated failure mechanism are favorable. Accordingly, the results obtained for the R-series specimens in the present study should be interpreted specifically as the response of the investigated smooth interface incorporating 8 mm-diameter reinforcing-bar connectors, rather than as a general assessment of the effectiveness of reinforcement across concrete–UHPC interfaces [15, 14]. Because the reinforcement area is approximately 50.27 mm^2, nominal bar-area ratios differ across models: 1.31%, 0.89%, and 1.03% at 20°, 30°, and 40°, respectively. These

differences, together with changing specimen aspect ratios and edge effects, limit isolation of the angle effect.

3.9 Cohesion, Friction, and Failure Envelope

The fitted apparent cohesion and friction coefficients are presented in Table 14 and illustrated in Figures 14 and 15. These are descriptive regression parameters from the tested loading configurations, not independently verified material constants.

3.10 Statistical Repeatability and Limitations

The scatter of the three replicate measurements at each angle is summarized in Table 13 and Figure 13. Only three distinct inclination-defined stress directions were examined, limiting the robustness and generalizability of the fitted envelopes.

3.11 Implications for UHPC Repair Applications

The experimental program reinforces the wider conclusion that UHPC can be a suitable repair material when the substrate interface is specifically designed. However, none of the results contain separate numerical groups for UHPC and a conventional repair material. Thus, what we present here is more direct evidence of interface geometry and preparation effects than of the interfacial material's superiority. Numerical comparisons between UHPC and classical repair concrete should be avoided unless appropriate material-related test data are available. For field use, substrate soundness, surface cleanliness, achievable groove geometry, curing, connector detailing and quality assurance must be considered jointly. The findings apply only to the tested C30–UHPC system and cannot be transferred quantitatively to other substrate classes or conventional repair mortars without validation. The pooled c and φ are descriptive test parameters, not directly transferable design values.

4. Conclusions

The confirmed peak loads were analyzed in kN and converted to nominal stresses using the actual gross cross-sectional area of each specimen and its specified interface inclination. The experimental program comprised 18 composite prisms, representing three interface inclinations (20°, 30°, and 40°), two interface configurations, and three replicates per configuration and angle. The substrate was C30 concrete, while UHPC served as the repair material. The results provide a controlled comparison of the two investigated configurations within the limitations of the adopted specimen geometry and loading method.

Across all three inclinations, the mechanically grooved, unreinforced interface configuration (G-series) exhibited higher mean axial failure stresses and calculated interfacial shear stresses than the nominally smooth interface containing an 8 mm reinforcing-bar connector (R-series). For example, at 30°, the mean calculated interfacial shear stresses were 12.65 MPa for the G-series and 10.91 MPa for the R-series. At 40°, the corresponding values were 14.27 MPa and 11.56 MPa. These comparisons support the practical importance of effective interface preparation for the tested concrete–UHPC repair assemblies; however, they do not demonstrate that grooving is universally superior to steel anchorage.

The interface angle altered the nominal normal and shear stress components derived from axial compression. Because the three angle groups also differed in square cross-sectional dimensions, the observed differences cannot be attributed to inclination alone. Furthermore, the experimental comparison changed two factors simultaneously: the G-series incorporated grooves without a connector, whereas the R-series incorporated a connector on a nominally smooth interface. The independent contributions of roughness and bar anchorage therefore remain unresolved.

The Mohr–Coulomb regressions offer a descriptive interpretation of the measured peak-load stress states rather than independently validated material constants. Replicate measurements quantify scatter within each inclination, but the three tested angles provide only three distinct stress-state directions. No interface slip was measured; consequently, interfacial stiffness, post-peak behavior,

fracture energy, and ductility cannot be inferred. Photographs document selected cracking and separation features but do not establish a complete failure-mode classification for every replicate.

Future investigations should use consistent specimen dimensions across interface angles and a factorial arrangement combining smooth and grooved surfaces with the presence and absence of connectors. Quantitative surface-roughness measurements, documented connector embedment, calibrated displacement instrumentation, and independently verified specimen failure classifications would strengthen causal interpretation and reproducibility. Additional loading conditions and replicate groups are recommended before transferring the reported apparent cohesion and friction parameters to structural design. Within these boundaries, the present results indicate that the investigated grooved configuration achieved greater peak bond-related resistance than the investigated bar-anchored configuration, highlighting the significance of substrate preparation in UHPC repair applications.

References

[1] Lyu J, Feng S, Zhang Q, Xiao H. Review of factors affecting bond strength between ultra-high-performance concrete and normal strength substrate. Construction and Building Materials. 2024;439:137416. https://doi.org/10.1016/j.conbuildmat.2024.137416

[2] Zhao L, Luo Q. Evaluating bonding strength in UHPC-NC composite: A comprehensive review of direct and indirect characterization methods. Construction and Building Materials. 2024;443:137701. https://doi.org/10.1016/j.conbuildmat.2024.137701

[3] Du W, Yang C, De Backer H, Li C, Ming K, Zhang H, et al. Experimental investigation on shear behavior of the interface between early-strength self-compacting shrinkage-compensating high-performance concrete and ordinary concrete substrate. Materials. 2022;15(14):4939. https://doi.org/10.3390/ma15144939

[4] Feng S, Xiao H, Li H. Comparative studies of the effect of ultrahigh-performance concrete and normal concrete as repair materials on interfacial bond properties and microstructure. Engineering Structures. 2020;222:111122. https://doi.org/10.1016/j.engstruct.2020.111122

[5] He S, Huang X, Huang J, Zhang Y, Wan Z, Yu Z. Shear bond performance of UHPC-to-NC interfaces with varying sizes: Experimental and numerical evaluations. Buildings. 2024;14(11):3684. https://doi.org/10.3390/buildings14113684

[6] He S, Huang X, Zhong H, Wan Z, Liu G, Xin H, et al. Experimental study on bond performance of UHPC-to-NC interfaces: Constitutive model and size effect. Engineering Structures. 2024;317:118681. https://doi.org/10.1016/j.engstruct.2024.118681

[7] Santos VB, Santos Silva APP, Poncetti BL, Tolentino LD, Krahl PA, Vanderlei RD. Influence of wetting conditions and concrete strength of both substrate and repair material on the bond capacity of repaired joints. Buildings. 2023;13(3):643. https://doi.org/10.3390/buildings13030643

[8] Wang Y, Qiao P, Sun J, Chen A, Yuan D, Wang Y. Influence of surface treatments and test methods on tensile strength of UHPC-NC interface bond. Construction and Building Materials. 2024;456:139051. https://doi.org/10.1016/j.conbuildmat.2024.139051

[9] Xu L, Yao Y, Li Y, Su J, Wu Y. Review of the interfacial bonding properties between ultrahigh-performance concrete and normal concrete. Applied Sciences. 2023;13(11):6697. https://doi.org/10.3390/app13116697

[10] Zhang B, Yu J, Chen W, Chen J, Li H, Niu J. Interface shear failure behavior between normal concrete (NC) and ultra-high performance concrete (UHPC). International Journal of Concrete Structures and Materials. 2024;18:18. https://doi.org/10.1186/s40069-023-00657-6

[11] Zhang B, Yu J, Chen W, Liu H, Li H, Guo H. Experimental study on bond performance of NC-UHPC interfaces with different roughness and substrate strength. Materials. 2023;16(7):2708. https://doi.org/10.3390/ma16072708

[12] Zhang Y, Zhu P, Liao Z, Wang L. Interfacial bond properties between normal strength concrete substrate and ultra-high performance concrete as a repair material. Construction and Building Materials. 2020;235:117431. https://doi.org/10.1016/j.conbuildmat.2019.117431

[13] Zhao YC, Lei HG, Guo LK, Lu GY. Experimental investigation on interface performance of UHPC-strengthened NC structure through push-out tests. Materials. 2023;16(5):1766. https://doi.org/10.3390/ma16051766

[14] Pei B, Yao H, Ye M, Wen Z, Wu TP, Li Y. Experimental study on interfacial bond performance between normal strength concrete (NSC) and ultra-high-performance concrete (UHPC). Construction and Building Materials. 2025;502:144478. https://doi.org/10.1016/j.conbuildmat.2025.144478

[15] Morthala RR, Shanmugam SP. Effect of surface preparation and shear links on the interface bond behaviour between ultra-high-performance and normal strength concrete. Engineering Structures. 2026;350:121965. https://doi.org/10.1016/j.engstruct.2025.121965
[16] Al-Abbas BH, Alsabbagh A, Hasan DM, Semendary AA, Aaleti S. Comparative studies on interfacial bond performance of ultrahigh performance concrete (UHPC) for sustainable repair of bridges and pavements. Results in Engineering. 2024;24:103525. https://doi.org/10.1016/j.rineng.2024.103525
[17] Feng S, Lyu J. The method of slant shear test with various slant shear angles decouple cohesion and friction of substrate-overlays interface. Construction and Building Materials. 2024;456:139238. https://doi.org/10.1016/j.conbuildmat.2024.139238